Asymmetric integrable turbulence and rogue wave statistics for the derivative nonlinear Schrödinger equation

Ming Zhong[1,2], Weifang Weng[3] and Zhenya Yan[*,4,2]

[1] School of Advanced Interdisciplinary Sciences, University of Chinese Academy of Sciences, Beijing 100049, China
[2] State Key Laboratory of Mathematical Sciences, Academy of Mathematics and Systems Science,

Chinese Academy of Sciences, Beijing 100190, China

[3] School of Mathematical Sciences, University of Electronic Science and Technology of China, Chengdu 611731, China

[4] School of Mathematics and Information Science, Zhongyuan University of Technology, Zhengzhou 450007, China

Abstract. We investigate a comprehensive analysis of asymmetric integrable turbulence and rogue waves (RWs) emerging from the modulation instability (MI) of plane waves for the derivative nonlinear Schrödinger (DNLS) equation. Over extended temporal evolution, a range of statistical measures are employed to assess the turbulence characteristics, including the n-th moments, ensemble-averaged kinetic and potential energy, wave-action spectrum, probability density function (PDF), and auto-correlation function. The n-th moments and ensemble-averaged kinetic and potential energy exhibit oscillatory convergence towards their steady-state values. Specifically, the amplitudes of oscillations for these indexes decay asymptotically with time as $t^{-1.36}$, while the phase shifts demonstrate a nonlinear decay with a rate of $t^{-0.78}$. The frequency of these oscillations is observed to be twice the maximum growth rate of MI. These oscillations can be classified into two distinct types: one is in phase with ensemble-averaged potential energy modulus $|\langle H_4 \rangle|$, and the other is anti-phase. At the same time, this unity is also reflected in the wave-action spectrum $S_k(t)$ for a given k, the auto-correlation function $g(x,t)$ for a given x, as well as the PDF $P(I,t)$ for a given $I = |\psi|^2$. The critical feature of the turbulence is the wave-action spectrum, which follows a power-law distribution of the form $|k + 3|^{-\alpha}$ expect for the finite value at $k = -3$. Unlike the NLS equation, the turbulence in the DNLS setting is asymmetric, primarily due to the asymmetry between the wave number of the plane wave from the MI and the perturbation wave number.. As the asymptotic peak value of S_k is observed at $k = -3$, the auto-correlation function exhibits a nonzero level as $x \to \pm L/2$. The PDF of the wave intensity asymptotically approaches the exponential distribution in an oscillatory manner. However, during the initial stage of the nonlinear phase, MI slightly increases the occurrence of RWs. This happens at the moments when the potential modulus is at its minimum, where the PDF becomes "fatter", and the probability of RWs occurring in the range of $I \in [12, 15]$ is significantly higher than in the asymptotic steady state.

Keywords: Integrable turbulence, Derivative nonlinear Schödinger equation, Modulation instability, Asymmetric turbulence, Rogue waves

Mathematics Subject Classification: 35Q51, 37K10, 65M99

1 Introduction

Weak wave turbulence (WWT) refers to a regime in which the interactions between waves are weakly nonlinear, leading to the gradual emergence of complex statistical behaviors over time [1–6]. This phenomenon typically arises in systems governed by non-integrable dispersive wave equations, where the wave resonance manifest in subtle energy exchanges [7–12]. One prototypical example is one-dimensional MMT

*Corresponding author. *Email address*: zyyan@mmrc.iss.ac.cn

model written as [13]:

$$i\psi_t = |\partial_x|^\alpha \psi + |\partial_x|^{\beta/4} \left(\left| |\partial_x|^{\beta/4} \psi \right|^2 |\partial_x|^{\beta/4} \psi \right),$$ (1)

where the envelope field $\psi = \psi(x,t)$ is a complex-valued function, the parameter β determines the degree of nonlinearity in the system, α governs the dispersion relation, which is given by $\omega(k) = |k|^\alpha$ with ω being the frequency and k the wave number. Unlike fluid turbulence, where the power law of the energy spectrum with respect to wave number is obtained through dimensional analysis, in WWT, Zakharov invented a method called the "Zakharov transform (ZT)" [1,2], which can derive specific power laws and obtain two dual cascades. The standard procedure typically involves employing the Fourier transform along with the assumption of independent Gaussian amplitudes and phases, which leads to the derivation of the wave-kinetic equation (WKE) [14]. Subsequently, the ZT was utilized to solve the equation analytically. A critical element in this approach is the existence of resonance manifolds. For the specific steps, one can refer to these books [1–3], which provides a detailed framework for deriving the WKE and applying the transform, along with the analysis of resonance manifolds.

However, the scenario significantly differs when considering integrable nonlinear dispersive equations, which represent a particularly important and distinctive type of nonlinear physical models, and possess significant theoretical value and practical relevance in the field of applied mathematics and mathematical physics, as well as related nonlinear science. The first key aspect is that the resonance manifolds will be empty [2,15,16], and the second one is that integrable nonlinear wave equations permit the existence of solitons, rogue waves (RWs), and other strongly nonlinear wave structures, which are characteristic of exact solutions in such systems. The concept of integrable turbulence (IT) was first introduced by Zakharov [15] to elucidate the failure of WWT theory in integrable nonlinear wave systems and to reveal a *novel turbulence mechanism*. This the IT concept describes the emergence of randomness and its statistical properties resulting from the long-term evolution of waves in integrable systems. The proposal of IT not only transcends the limitations of traditional WWT, but also provides a new perspective for understanding the complex dynamical behaviors of nonlinear wave systems. Consequently, it has sparked extensive research interest in both theoretical and experimental fields [17–42], mostly focusing on one-dimensional integrable nonlinear Schrödinger equation (NLSE), expressed as [2,43–45]:

$$\begin{cases} i\psi_t + \psi_{xx} + |\psi|^2\psi = 0, \\ \psi(x,0) = \psi_0(x), \end{cases}$$ (2)

serving as a fundamental model, holding significant importance in various disciplines such as quantum mechanics, nonlinear optics, fluid dynamics, deep ocean, plasma physics, and Bose-Einstein condensates (BECs).

Serving as another fundamental and widely studied nonlinear physical model with diverse applications in various fields, the derivative nonlinear Schrödinger equation (DNLSE) [46–53],

$$i\psi_t + \psi_{xx} + ig(|\psi|^2\psi)_x = 0, \quad g \in \mathbb{R}$$ (3)

describes the evolution of wave phenomena in nonlinear and dispersive media. For example, it characterizes the propagation of circularly polarized nonlinear Alfvén waves in plasmas [46,48,51–53] and describes the dynamics of weakly nonlinear electromagnetic waves in ferromagnetic [54], anti ferromagnetic [55], or dielectric [56] systems subjected to an external magnetic field. The DNLSE (3) is completely integrable and

associated with the following modified Zakharov-Shabat eigenvalue problem [49]:

$$\Phi_x = X\Phi, \quad X = X(x,t;\lambda) = i\lambda^2\sigma_3 + \lambda Q, \tag{4}$$

$$\Phi_t = T\Phi, \quad T = T(x,t;\lambda) = -\left(2\lambda^2 + Q^2\right)X - i\lambda Q_x\sigma_3, \tag{5}$$

where $\Phi = \Phi(x,t;\lambda)$ is a 2×2 matrix-valued eigenfunction, $\lambda \in \mathbb{C}$ is a spectral parameter, the potential matrix $Q = Q(x,t)$ is written as

$$Q(x,t) = \begin{bmatrix} 0 & \psi(x,t) \\ g\psi^*(x,t) & 0 \end{bmatrix}, \tag{6}$$

the asterisk $(*)$ denotes the complex conjugate, and σ_3 is one of Pauli's spin matrices given by

$$\sigma_1 = \begin{bmatrix} 0 & 1 \\ 1 & 0 \end{bmatrix}, \quad \sigma_2 = \begin{bmatrix} 0 & -i \\ i & 0 \end{bmatrix}, \quad \sigma_3 = \begin{bmatrix} 1 & 0 \\ 0 & -1 \end{bmatrix}. \tag{7}$$

The DNLSE (3) is just the compatibility condition (or the zero-curvature condition), $X_t - T_x + [X, T] = 0$ of system (4)-(5).

Abundant localized wave structures, such as solitons, rogue waves, and breathers, have been discovered for the DNLSE (3) [57–61]. The parameter g represents the relative strength of the derivative nonlinear term. For simplicity, we can assume $g = 1$, since the case where $g = -1$ can be transformed into $g = 1$ by applying the coordinate transformation $x \rightarrow -x$. The DNLSE (3) with $g = 1$ can be expressed in Hamiltonian form as follows [49]:

$$\frac{\partial \psi}{\partial t} = \frac{\partial}{\partial x}\frac{\delta H}{\delta \psi^*}, \tag{8}$$

with

$$H\left(\psi\right) = H_k + H_4, \tag{9}$$

where the kinetic energy (similar to the NLSE [18, 19]) is

$$H_k = -\frac{i}{2}\int_{-\infty}^{\infty}\left(\psi\psi_x^* - \psi_x\psi^*\right)dx \tag{10}$$

and the potential energy is

$$H_4 = -\frac{1}{2}\int_{-\infty}^{\infty}|\psi|^4dx. \tag{11}$$

One can easily verify that the Hamiltonian in Eq. (9) is a conserved quantity. Another important conserved quantity is the mass given by:

$$N(\psi) = \int_{-\infty}^{\infty}|\psi|^2dx. \tag{12}$$

A key mechanism in the NLSE (2) for generating IT [18] refers to modulation instability (MI, alias Benjamin-Feir instability) [62–64]. In the noise-induced MI model of NLSE (2), the plane-wave solution is typically augmented by a small stochastic perturbation:

$$\psi_0(x) = 1 + \xi(x), \tag{13}$$

where $\xi(x)$ represents a small noise with $\langle|\xi|^2\rangle \ll 1$ and zero average, $\langle\xi\rangle = 0$. Here, $\langle\cdot\rangle$ denotes the averaging over multiple realizations of the noise. Mathematically, the average is given by

$$\langle\xi\rangle = \int \xi p(\xi)d\xi = 0, \tag{14}$$

where $p(\xi)$ is the probability density function (PDF) of noise ξ. It should be noted that for the NLSE, the initial condition with $\psi_0(x)$ is in the MI region. Under the influence of MI, the initial plane wave evolves into a chaotic wave field, which can be characterized by robust statistical metrics [18,20,23,26,28,30,34,35,37]. In such a steady-state wave field, various sophisticated localized wave structures emerge [64,65], increasing the complexity and richness of wave dynamics. The interactions and collisions among these structures lead to the appearance of high-amplitude waves, commonly referred to as rogue waves (RWs) [66–68].

The study of RWs in chaotic wave fields has become a prominent area of research in nonlinear science. RWs were first observed in deep ocean, where they manifest as unusually large amplitude waves that appear unexpectedly [44,69–71]. Characterized by tall peaks, deep troughs, and transient behavior, RWs typically last only a few seconds [72,75,76,78–84]. Their study has extended beyond oceanography to various other domains, demonstrating their universal presence. For example, rogue wave-like phenomena have been observed in nonlinear optical fibers [67,85], quantum fluids in superfluid mechanics [86], and in plasma physics [87,88], highlighting the widespread relevance of RWs. The RW phenomenon also appears in other fields, such as BECs [89,90], Alfvén waves [91], and even finance [92]. RW generation can be driven by a variety of mechanisms, ranging from simple linear effects to complex nonlinear interactions within non-zero backgrounds. One approach to understanding RW generation is through the study of MI and IT [18,20,34,72–74,77,79,84,93–97].

Inspired by the NLSE, a natural issue arises: does MI in the DNLSE (3) lead to the formation of turbulence? In this case, how does the resulting turbulence differ from the one observed in the NLSE (2) [18,19]? In this paper, we aim to systematically investigate turbulence phenomena within the framework of the DNLSE (3), along with the formation of RWs. To achieve this aim, we perform an extensive set of numerical simulations of the DNLSE (3), using the initial condition provided in Eq. (24). The key contributions of this paper can be summarized as follows:

- We carefully explore the relationship between MI and RWs in the DNLSE (3), and compared the RWs generated by the MI of plane waves with the exact one.

- We broaden the concept of IT to encompass the DNLSE (3), offering a thorough examination of IT within this framework. Through various statistical measures, we identify the occurrence of stationary IT in the DNLSE (3).

- We find that, unlike the symmetric turbulence observed in the NLSE, the turbulence in the DNLSE exhibits anisotropy, with the power-law behavior varying in different regions.

The rest of this paper is arranged as follows. In Sec. 2, we derive the wave number range satisfied by the unstable plane waves using MI theory, and examine their relationship with the exact RWs in the DNLSE (3). In Sec. 3, we carefully analyze the evolution of various statistical indices during the onset of turbulence, as well as the asymptotic steady state. Finally, some conclusions and discussions are presented in Sec. 4.

2 Modulation instability and rogue waves

Prior to investigating IT, it is essential to first assess the MI of the plane wave solutions [62–64], thereby facilitating the generation of IT. A direct verification shows that the DNLSE (3) admits the following plane-

wave solutions:

$$\psi(x,t) = Ae^{i(kx-wt)}, \quad w = k^2 + A^2 k, \tag{15}$$

where $A > 0$ is the constant amplitude, and $k \in \mathbb{R}$ is the wave-number, and w the frequency of the plane wave. We commence with a rigorous examination of the linear stability of plane wave solutions Eq. (15) to the DNLSE (3), exploring their susceptibility to perturbations via adding small disturbance as $\psi(x,t) = (A + \epsilon(x,t)) e^{i(kx-wt)}$, with $|\epsilon(x,t)| \ll 1$. Upon substituting into Eq. (3) and linearizing with respect to $\epsilon(x,t)$, we derive the governing equation for $\epsilon(x,t)$:

$$i\epsilon_t + \epsilon_{xx} + i(2k\epsilon_x + 2A^2\epsilon_x + A^2\epsilon_x^*) - kA^2(\epsilon + \epsilon^*) = 0. \tag{16}$$

Let the perturbation $\epsilon(x,t)$ be assumed to have a solution in a linear superposition of plane waves:

$$\epsilon(x,t) = \delta_1 e^{i(Qx - \Omega t)} + \delta_2^* e^{-i(Qx - \Omega^* t)}, \tag{17}$$

where $\delta_\ell \, (\ell = 1,2), Q, \Omega$ represent the constant amplitudes, wave-number, as well as frequency, respectively. Furthermore, it is readily apparent that MI arises if the imaginary part of the disturbance frequency Ω is nonzero. By substituting Eq. (17) into Eq. (16), we derive that the necessary and sufficient condition for the existence of a nontrivial solution $((\delta_\ell, , \ell = 1,2) \neq 0)$ is that the determinant of the coefficient matrix M vanishes, where

$$M = \begin{pmatrix} \Omega + w - (k+Q)^2 - 2A^2(Q+k) & -A^2(k+Q) \\ -A^2(k-Q) & -\Omega + w - (k-Q)^2 - 2A^2(k-Q) \end{pmatrix}. \tag{18}$$

Therefore, the necessary and sufficient condition for the instability of the plane wave given by Eq. (15) is:

$$\Delta = A^4 + 2A^2 k + Q^2 < 0. \tag{19}$$

Moreover, for the plane wave with $k < -\frac{A^2}{2}$, MI manifests, and the corresponding unstable growth rate (i.e., the imaginary part of Ω) is given by:

$$G = Q\sqrt{-A^4 - 2A^2 k - Q^2}. \tag{20}$$

It is straightforward to determine that the maximum instability (with maximum absolute value of G) occurs when the disturbance wave number is given by:

$$Q_{\max} = \pm\sqrt{\frac{-A^2(2k + A^2)}{2}}, \tag{21}$$

and the maximum growth rate of the instability,

$$G_0 = \frac{-A^2(2k + A^2)}{2}. \tag{22}$$

Therefore, the characteristic length of the instability is $\lambda = 2\pi/|Q_{\max}|$, and the characteristic time is $\tau = 1/G_0$.

Now, we proceed with a numerical verification of MI and its relationship with RWs. Initially, we assign the amplitude of the plane wave parameter as $A = 1$. Hence, MI occurs at
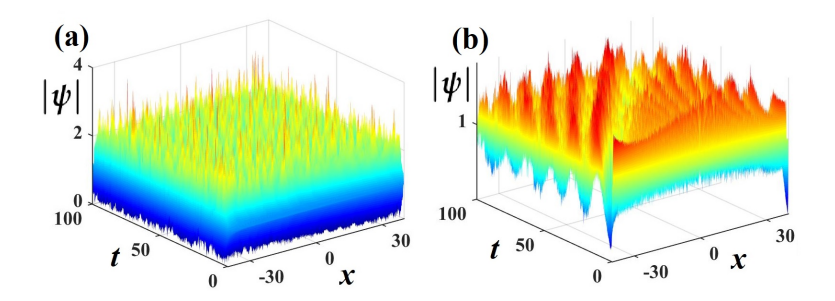
$$k < -\frac{1}{2}. \tag{23}$$

5

Figure 1: A typical evolution of the turbulent wave field $|\psi(x,t)|$ for a single realization corresponds to the parameters at MI region (*a*) with $k = -3$, and at MS region (*b*) with $k = -1/4$.
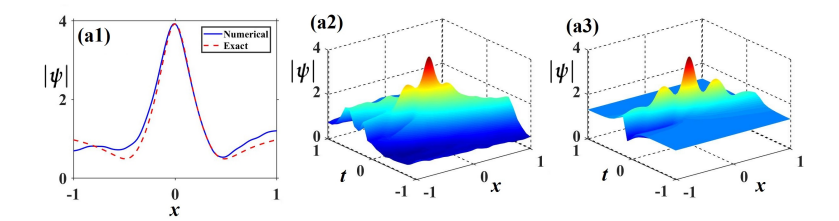

Figure 2: The largest RWs detected in the realization corresponding to figure 1(a). (*a1*) The comparison between the largest RW detected in the realization and the cross-profile of exact RW solution, where the blue solid and red dashed lines represent the numerical and exact ones, respectively. The space-time representation near the location where the maximum amplitude is attained of numerical realization at (*a2*) and exact solution at (*a3*). To enhance visualization, we translate the point of maximum amplitude to the coordinates $(x,t) = (0,0)$.

The numerical results are shown in figure 1, with the parameter k being located in the MI region at $k = -3$ in panel (*a*), and in the modulation stable (MS) region at $k = -1/4$ in panel (*b*). The numerical results provide a strong validation for the theory. We observe that in the MI region (see figure 1(*a*)), the amplitude of the plane wave increases significantly due to the instability, reaching values greater than 3. In contrast, in the MS region (see figure 1(*b*)), the amplitude does not experience significant growth over time. It should be noted here that the linear instability we consider does not cause the ill-posedness of the solution [98].

Subsequently, we investigate the relationship between MI and RWs. In figure 2, we present the largest extreme RW event detected in the realization corresponding to figure 1(*a*). The comparison between the detected one and exact RW with parameters $\alpha = 0.95, \beta = 0.5$ (see Eq. (55) in [59]) is displayed in figure 2(*a1*), which exhibits a noticeable level of consistency. The space-time representation near the location of the maximum amplitude, shown for the numerical realization in figure 2(*a2*) and the exact solution in figure 2(*a3*). Due to the instability induced by MI, the localization of the RW in figure 1(*a2*) is slightly less precise; however, a general agreement with the exact RW can still be observed.

3 Formation of asymmetric integrable turbulence

First, building upon the stability analysis presented in the preceding section, we examine the DNLSE (3), with the initial conditions specified as:

$$\psi(x,0) = e^{-3ix}\left(1 + \text{noise}\right), \tag{24}$$
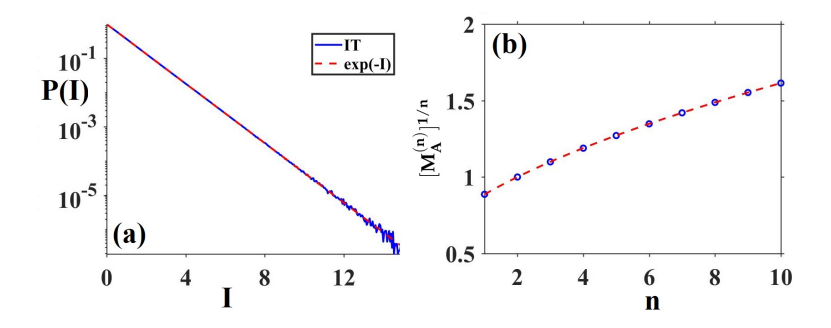
6

Figure 3: (a) The PDF of intensity $I = |\psi|^2$, where the blue solid line represents asymptotic state of IT, while the red dashed line denotes the exponential distribution $\exp(-I)$. (b) The asymptotic values of the moments $M_A^{(n)}$, where $n = 1, \ldots, 10$, are represented by blue circles. These values are compared with the Rayleigh prediction, $\Gamma\left(\frac{n}{2} + 1\right)$, which is shown as a dashed red line.
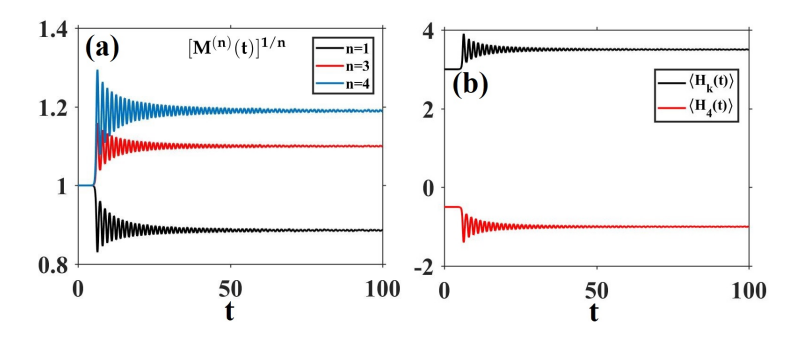

Figure 4: (a) The evolution of n-th moment $\left[M^{(n)}(t)\right]^{1/n}$ (see Eq. (25)) ($n = 1, 2, 3$) with time t. (b) The evolution of ensemble-averaged kinetic energy $\langle H_k(t) \rangle$ Eq. (10) and potentia energy $\langle H_4(t) \rangle$ Eq. (11) with time t.

that is, $A = 1$, $k = -3$ in the plane-wave solution in Eq. (15), which lies within the parameter regime of MI. Note that the initial conditions here can also be adjusted, as long as the parameters remain within the range of MI. The initial condition contains a random perturbation in the form of small-amplitude Gaussian noise. Considering IT, we will analyze it using the following different statistical indexes in this section. And the IT will be characterized from two distinct perspectives: first, by examining the steady-state values of its statistical metrics, and second, by analyzing the dynamical evolution of these metrics as they approach to their equilibrium states. For details of the specific numerical algorithm, readers are referred to Appendix 4.

3.1 Moments and probability density function

An essential statistical measure in this context is the fourth-order moment, which is directly linked to kurtosis, derived from the initial conditions given in Eq. (24). This quantity provides crucial insights into the distribution's peakedness and tail behaviors, which are vital for understanding the formation of rogue waves in the turbulent regime of nonlinear wave dynamics [18, 19]. The general expression for the n-th moment is given by:

$$M^{(n)}(t) = \left\langle \frac{1}{L} \int_{-L/2}^{L/2} |\psi(x, t)|^n \, dx \right\rangle. \tag{25}$$
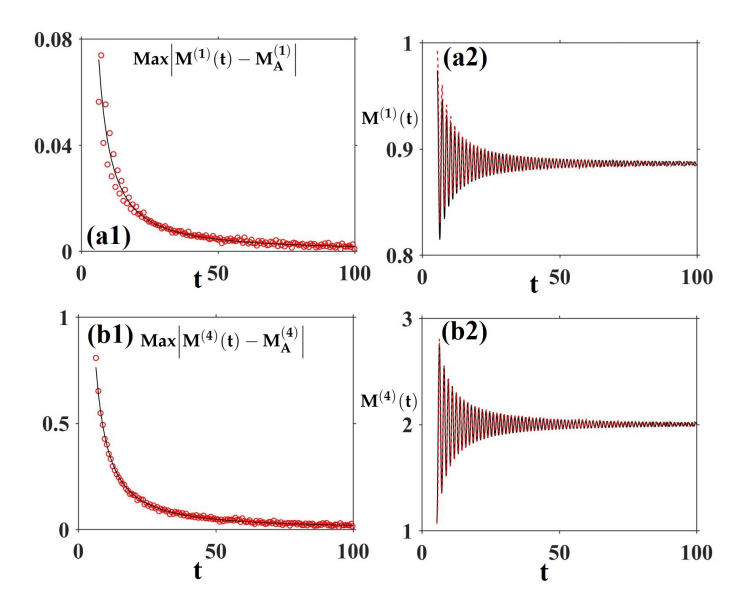
Figure 5: (*a1*) The magnitude of the deviations of the extreme of $M^{(1)}(t)$ from its asymptotic value $M_A^{(1)}$, as a function of time t. (*a2*) The evolution of the moment $M^{(1)}(t)$ (solid black line) is fitted by the function $M_A^{(1)} + \frac{a_1}{t^{\alpha_1}} \sin\left(b_1 t + c_1/t^{\beta_1} + \theta_0^{(1)}\right)$, with the parameters $M_A^1 \approx 0.886$, $\{a_1, \alpha_1, b_1, c_1, \beta_1, \theta_0^{(1)}\} \approx \{0.89, 1.36, 4.89, 51.41, 0.78, -44.59\}$ (dashed red line). (*b1*) The same as (a1), expect $M^{(1)}(t)$ is changed into $M^{(4)}(t)$. (*b2*) The same as (a2), expect $M^{(1)}(t)$ is changed into $M^{(4)}(t)$, as well as the parameters $M_A^4 \approx 2$, $\{a_2, \alpha_2, b_2, c_2, \beta_2, \theta_0^{(2)}\} \approx \{9.39, 1.35, 4.89, 51.06, 0.80, -41.46\}$.

It is worth noting that the second moment, $M^{(2)}(t) \equiv M^{(2)}(0) \approx 1$, reflects the DNLSE (3), which holds true throughout the evolution. Indeed, Eq. (25) can be rewritten in the form of PDF as shown below:

$$M^{(n)}(t) = \int_0^{+\infty} |\psi|^n \mathcal{P}(|\psi|, t) d|\psi|. \tag{26}$$

If the PDF of wave amplitudes coincides with Rayleigh distribution:

$$P_{Ra}\left(|\psi|\right) = 2|\psi| e^{-|\psi|^2}, \tag{27}$$

then it can be shown that the *n*-th moment, $M_{Ra}^{(n)}(t)$, is given by $\Gamma\left(\frac{n}{2} + 1\right)$. By performing a variable substitution $I = |\psi|^2$, the PDF of the intensity I can be obtained as $P_{Ra}\left(I\right) = \exp(-I)$, which is called the exponential distribution.

As depicted in figure 3(*a1*), the asymptotic PDF of the intensity, $P(I)$, matches the exponential PDF, $\exp(-I)$. This observation leads to a rather unexpected conclusion: although the DNLSE (3) is inherently nonlinear, its asymptotic PDF is indistinguishable from that of a wave field governed by a linear equation. To further corroborate this finding, we computed the asymptotic values of the moments $M_A^{(n)}$, and discovered that they are in good agreement with the Rayleigh predictions for $n = 1, ..., 10$, as illustrated in figure 3(*b*). Furthermore, we discovered the following relationship between the ensemble average potential energy H_4 and the fourth-order moment as

$$\langle H_4 \rangle = -\frac{1}{2} M_A^{(4)} = -1. \tag{28}$$

Therefore, the asymptotic value of ensemble average kinetic energy $\langle H_k \rangle = \frac{7}{2}$ since the conservation of ensemble average Hamiltonian $\langle H \rangle = \langle H_k \rangle + \langle H_4 \rangle = \frac{5}{2}$. The nonlinearity degree in asymptotic state of IT

8

can be estimated using the following parameter:

$$R = \frac{|\langle H_4 \rangle|}{\langle H_k \rangle} = \frac{2}{7}. \tag{29}$$

In the case of WWT, where $|R| \ll 1$, the Rayleigh PDF naturally arises as the expected outcome. However, for the DNLSE, we observe a regime of "slightly strong" turbulence in the asymptotic state, with $R = 2/7$. This suggests a shift from the WWT regime, indicating a significant increase in nonlinearity as the system evolves.

The relation given in Eq. (28) is particularly noteworthy. Referring to Eq. (11), we can write:

$$-\langle H_4 \rangle = \frac{1}{2} \sum_{k_1, k_2, k_3, k_4} \langle \psi_{k_1} \psi_{k_2} \psi_{k_3}^* \psi_{k_4}^* \rangle \delta_{k_1 + k_2 - k_3 - k_4},$$

where ψ_{k_i} is the Fourier transform as defined in Eq. (42), δ_k is the Kronecker delta function defined as:

$$\delta_k = \begin{cases} 1, & \text{if } k = 0, \\ 0, & \text{if } k \neq 0. \end{cases} \tag{30}$$

The four-point correlation, or four-wave momentum, can be rewritten as [8, 18, 19]:

$$\langle \psi_{k_1} \psi_{k_2} \psi_{k_3}^* \psi_{k_4}^* \rangle = I_{k_1} I_{k_2} \left(\delta_{k_1 - k_3} \delta_{k_2 - k_4} + \delta_{k_1 - k_4} \delta_{k_2 - k_3} \right) + J_{k_1, k_2, k_3, k_4}, \tag{31}$$

where J_{k_1, k_2, k_3, k_4} represents the cumulant, I_{k_i} denotes the wave-action spectrum (see Eq. (41)). Noting that the sum of I_k terms is approximately the mean mass, $\sum I_k = \langle N \rangle \approx 1$, we obtain the following approximation:

$$-\langle H_4 \rangle \approx 1 + \frac{1}{2} \sum_{k_1, k_2, k_3, k_4} J_{k_1, k_2, k_3, k_4} \delta_{k_1 + k_2 - k_3 - k_4}. \tag{32}$$

When we combine this with the relation from Eq. (28), we get:

$$\left| \sum_{k_1, k_2, k_3, k_4} J_{k_1, k_2, k_3, k_4} \delta_{k_1 + k_2 - k_3 - k_4} \right| \ll 1. \tag{33}$$

This inequality suggests that, in the asymptotic limit of the turbulent state, the cumulant J_{k_1, k_2, k_3, k_4} tends to zero. Therefore, the fact that $\langle H_4 \rangle \approx -1$ strongly implies that the turbulence is Gaussian in nature in its stationary state.

To investigate the evolution towards the asymptotic turbulent state, as displayed in figure 4, we examine the moments $M^{(n)}(t)$, the ensemble-averaged kinetic energy $\langle H_k \rangle$, potential energy $\langle H_4 \rangle$. Initially, up to $t \sim 5$, the perturbations to the condensate are minimal, resulting in only slight variations from their initial values: $M^{(n)} \approx 1$, $\langle H_k \rangle \approx 3$, and $\langle H_4 \rangle \approx -1/2$. At around $t \sim 5$, the MI transforms into its nonlinear phase, marking a significant shift. During this phase, the moments start to oscillate about their asymptotic Rayleigh values $\Gamma(n/2 + 1)$, with the kinetic energy stabilizing at approximately $7/2$, and the potential energy around -1.

Remarkably, the moment $M^{(1)}(t)$ exhibits in-phase oscillations with the potential energy $\langle H_4 \rangle$, while it oscillates out of phase with the higher-order moments $M^{(n)}(t)$ (for $n \geq 3$) and the kinetic energy $\langle H_k \rangle$ during the transition from the nonlinear stage of MI to the asymptotic state. Consequently, the temporal positions of the local maxima and minima of $M^{(1)}(t)$ and $\langle H_4 \rangle$ coincide, aligning precisely with the local
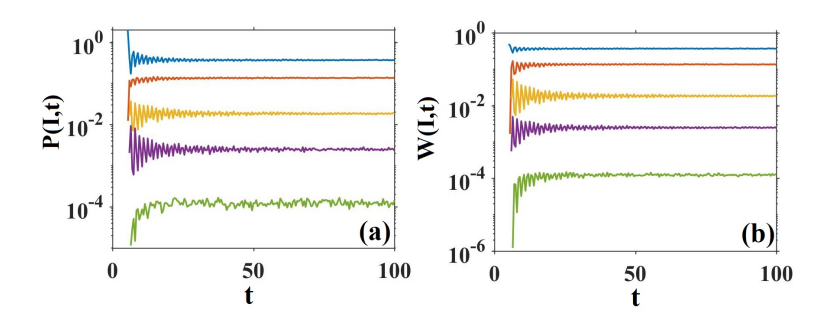
9

Figure 6: (*a1*) Evolution of PDF $P(I, t)$ for specific I, $I = 1$ (blue), $I = 2$ (red), $I = 4$ (yellow), $I = 6$ (purple), $I = 9$ (green). (*a2*) Similar with panel (a1) expect the PDF $P(I, t)$ is replaced by cumulative probability $W(K, t)$.

minima and maxima of $M^{(n)}(t)$ (for $n \geq 3$) and $\langle H_k \rangle$, respectively. This intricate phase relationship reveals the underlying dynamics governing the evolution of turbulence in this system. In fact, the result can be derived from a relatively straightforward perspective. First, it is important to note that $\Gamma(n/2 + 1) \leq 1$ holds if and only if $n \leq 2$. Since the initial values of all n-th moments are unity, it follows that $M^{(1)}(t)$ initially decreases, while the higher-order moments $M^{(n)}(t)$ (for $n \geq 3$) increase. A similar analysis can be applied to the kinetic energy $\langle H_k \rangle$ and the potential energy $\langle H_4 \rangle$, with the crucial observation that the Hamiltonian is conserved throughout the process.

We investigate the time dependence of the oscillations using the examples of the moments $M^{(1)}(t)$ and $M^{(4)}(t)$. figure 5(*a1*) reveals that the oscillatory amplitude of $M^{(1)}(t)$, defined as the absolute deviation of its extreme from the asymptotic value $M_A^{(1)}$, exhibits a power-law decay governed by the scaling relation a_1/t^{α_1}, with a numerically determined prefactor $a_1 = 0.89$ and the power $\alpha_1 = 1.36$. Notably, the oscillation period undergoes a progressive reduction over time, decreasing from $T \sim 1.5$ at $t \sim 10$ to $T \sim 1.3$ at $t \sim 100$. This temporal compression of the period is reminiscent of a nonlinear phase shift. Hence such behavior suggests that the temporal evolution of $M^{(1)}(t)$ can be effectively captured by a tailored functional form as:

$$M^{(1)}(t) \approx M_A^{(1)} + \frac{a_1}{t^{\alpha_1}} \sin\left(\theta^{(1)}(t)\right), \quad \theta^{(1)}(t) = b_1 t + \theta_{nl}^{(1)}(t) + \theta_0^{(1)}, \tag{34}$$

where $\theta^{(1)}(t)$ is the phase due to the existence of periodic oscillation, including frequency b_1, nonlinear phase shift $\theta_{nl}^{(1)}(t)$ as well as initial phase $\theta_0^{(1)}$. It is worth mentioning that the nonlinear phase shift is also a power function of time t, i.e., $\theta_{nl}^{(1)}(t) = c_1/t^{\beta_1}$ with $\beta_1 = 0.78$. Indeed, the parameters a_1 and α_1 can be determined by identifying the extreme of $|M^{(1)}(t) - M_A^{(1)}|$, as clearly illustrated in figure 5(*a1*). Then the parameters $\{b_1, c_1, \theta_0^{(1)}\}$ can be determined by the following conditions:

$$\theta\left(t_{\max}^m\right) = b_1 t_{\max}^m + \theta_{nl}(t_{\max}^m) + \theta_0 = \frac{3\pi}{2} + 2\pi m \tag{35}$$

with $m = 0, 1, 2$, and $t_{\max}^m$ represents the deviations of local maximums of $M^{(1)}(t)$ from it's asymptotic value $M_A^{(1)}$. Then the parameters can be identified as $\{4.89, 51.41, -44.59\}$. The evolution of $M^{(1)}(t)$ and the corresponding fitting function Eq. (34) are depicted in figure 5(*a2*), which reveals a strong alignment.

Analogously, we could investigate the variations of $M^{(4)}(t)$ and the associated fitting function as:

$$M^{(4)}(t) \approx M_A^{(4)} + \frac{a_2}{t^{\alpha_2}} \sin\left(\theta^{(2)}(t)\right), \quad \theta^{(2)}(t) = b_2 t + \theta_{nl}^{(2)}(t) + \theta_0^{(2)}, \tag{36}$$
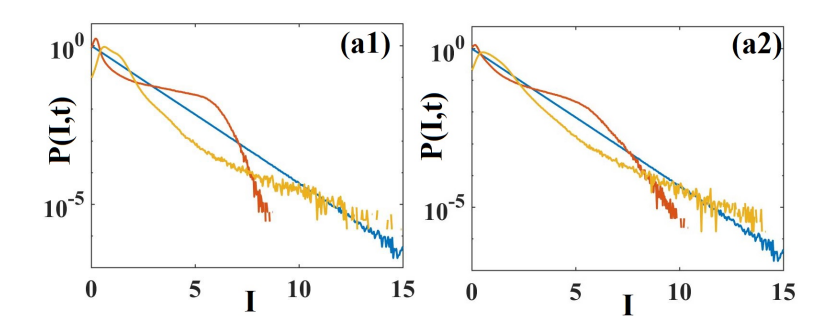
10

Figure 7: (*a1*) The PDF of intensity, $P(I, t)$, at $t = 6.4$, corresponding to the first local maximum of the ensemble-averaged potential energy modulus $|\langle H_4 \rangle|$ (red line); at $t = 7.3$, corresponding to the first local minimum of $|\langle H_4 \rangle|$ (yellow line); and as the asymptotic spatial correlation function (blue line). (*a2*) The PDF of intensity, $P(I, t)$, at $t = 8.1$, corresponding to the second local maximum of the ensemble-averaged potential energy modulus $|\langle H_4 \rangle|$ (red line); at $t = 8.9$, corresponding to the second local minimum of $|\langle H_4 \rangle|$ (yellow line); and as the asymptotic spatial correlation function (blue line).

with $\theta_{nl}^{(2)}(t) = c_2/t^{\beta_2}$ with $\beta_2 = 0.8$. It is evident that β_1 and β_2 exhibit remarkable similarity, and this discrepancy could potentially be rectified with a greater volume of ensembles. The parameters $\{a_2, \alpha_2, b_2, c_2, \theta_0^{(2)}\}$ are numerically found as $\{9.39, 1.35, 4.89, 51.06, -41.46\}$. It is observed that the parameters $\{\alpha_2, b_2, c_2\}$ are very close to $\{\alpha_1, b_1, c_1\}$, which is natural. However, the difference between a_2 and a_1 is more pronounced. This can be attributed to the fact that $M^{(4)}(t)$ deviates significantly from its asymptotic steady-state value when initially entering the nonlinear MI phase, in contrast to $M^{(1)}(t)$. Meanwhile, we have

$$\theta_0^{(1)} \approx \theta_0^{(2)} + \pi, \tag{37}$$

which arises from their anti-phase evolution, resulting in the observed effect. The results are presented in figure 5(*b1,b2*). As for the evolution of other moments, the ensemble-averaged kinetic energy $\langle H_k \rangle$ as well as the potential energy $\langle H_4 \rangle$ can be similarly obtained. Note that in the case of $A = 1, k = -3$, we have

$$Q_{\max} = \pm\sqrt{5/2}, \quad G_0 = 5/2. \tag{38}$$

Similar with the work in [18], we have $b_1 = b_2 \approx 2G_0$, and we find that the frequency b_1 or b_2 should coincide with 5 if we consider lager ensembles.

Next, we will carefully investigate the time evolution of $P(I, t)$ for the specific $I = |\psi|^2$, where the results for $I = \{1, 2, 4, 6, 9\}$ are exhibited in figure 6(*a1*). It can be observed that the evolution is in-phase or anti-phase with that of ensemble-averaged potential energy modulus $|\langle H_4 \rangle|$ (see figure 5(*b2*) but with different values). We opt for the absolute value of the ensemble-averaged potential energy, as its local maximal and minimal correspond to the moments of strongest and weakest effects, respectively. Then in phase means that the statistic index take local maximal values at the local maximums of potential energy modulus $|\langle H_4 \rangle|$, and local minimal values at the local minimums of $|\langle H_4 \rangle|$. The anti-phase relationship is the opposite. It is noted that during the linear MI stage, the probability density at $I = 1$ is significantly greater than at other intensities. As the nonlinear MI develops, $P(1, t)$ will approach its asymptotic value in an inversely proportional manner to $|\langle H_4 \rangle|$. Meanwhile, $P(2, t)$, $P(4, t)$, and $P(6, t)$ also approach their respective asymptotic values, in phase with $|\langle H_4 \rangle|$. However, the evolution of $P(9, t)$ is more erratic, as $I = 9$ corresponds to a rare event.

The probability of waves exceeding a certain threshold $I > K$ is given by the cumulative probability $W(K, t)$, which can be expressed as:

$$W(K, t) = \int_{K}^{+\infty} P(I, t) \, dI. \tag{39}$$

Note that in case of the Rayleigh PDF in Eq. (27), this probability takes the simple form

$$W(K, t) = e^{-K}. \tag{40}$$

The results for $K = \{1, 2, 4, 6, 9\}$ are summarized in figure 6($a2$), where similar oscillations can be observed. For the final state, we compared our numerical results with the theory in Eq. (40) and found a very good agreement, with an error on the order of 10^{-4}.

Next, we consider $P(I, t)$ in the cases of the local maxima and minima of the ensemble-averaged potential energy modulus. As depicted in figure 7($a1$), it is observed that at the first local maximal time ($t = 6.4$), the PDF surpasses the asymptotic distribution within the interval $I \in [3, 7]$, a region identified as the "imperfect rogue wave" [18] (see also figure 7($a2$) at $t = 8.1$). Due to the influence of MI, the "imperfect" rogue waves typically appear at the first few local maxima of $|\langle H_4 \rangle|$. In spatial terms, these waves form a modulated lattice structure, consisting of large waves, as displayed in figure 8(a1,a3) with time $t = 6.4$ and $t = 8.1$, which correspond to the first and second moment of local maxima. Next, we focus on the first two moments of local minimum values of $|\langle H_4 \rangle|$, as illustrated in figure 7($a1,a2$). In the range of $12 \leq I \leq 15$, the PDF at these instances surpasses the asymptotic PDF. These waves are uncommon occurrences, emerging in the context of a disturbed wave field (see a typical spatial distribution with $t = 7.3, 8.9$ at figure 8($a2,a4$)), which generally has an amplitude smaller than $I < 4$. Due to the influence of the PDF, during the early stages of nonlinear MI, at the moments corresponding to the local maxima of $|\langle H_4 \rangle|$, the wave-action spectrum $S_k(t)$ has more peaks but smaller peak values, compared to the moments corresponding to the local maxima of $|\langle H_4 \rangle|$. A similar phenomenon also occurs in the auto-correlation function $g(x, t)$, which is due to the the wave field is less correlated.

3.2   Wave-action spectrum and auto-correlation function

In this subsection, we aim to examine the asymptotic behavior of the wave-action spectrum $S_k(t)$ and the auto-correlation function $g(x, t)$, as well as their progression toward the final state. The wave-action spectrum $S_k(t)$ can be defined as

$$S_k(t) = \langle |\psi_k(t)|^2 \rangle. \tag{41}$$

The quantity $\psi_k(t)$, defined as the semi-discrete Fourier transform, differs from its continuous counterpart primarily because periodic boundary conditions are imposed by the numerical methods we use. These transforms are expressed as:

$$\psi_k(t) = \mathcal{F}_D[\psi(x, t)] = \frac{1}{L} \int_{-L/2}^{L/2} \psi(x, t) e^{-ikx} \, dx,$$

$$\psi(x, t) = \mathcal{F}_D^{-1}[\psi_k(t)] = \sum_k \psi_k(t) e^{ikx}. \tag{42}$$

To distinguish them from the continuous Fourier transforms, we denote them as $\mathcal{F}_D$ and $\mathcal{F}_D^{-1}$. Here, the length $L = 2m\pi$, where $m \gg 1$ is a large integer, and the wave number is defined as $k = 2n\pi/L$ with n
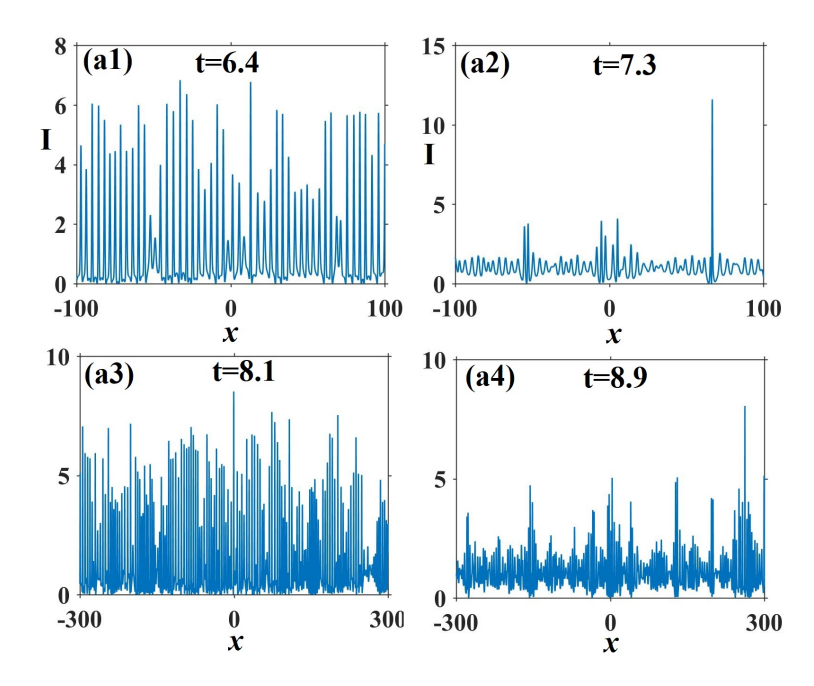
Figure 8: Spatial distribution of the intensity $I = |\psi|^2$ at (*a1*) $t = 6.4$, (*a2*) $t = 7.3$, (*a3*) $t = 8.1$ as well as (*a4*) $t = 8.9$ for single realization.

being an integer. The wave-action spectrum is the spectral density of wave action since

$$\langle N \rangle = \sum_k S_k(t). \tag{43}$$

According to Eq. (42), all wave-action spectrum of the initial condition in Eq. (24) is concentrated in the $k = -3$ harmonic,

$$I_k = \begin{cases} 1, & k = -3, \\ 0, & k \neq -3. \end{cases} \tag{44}$$

According to the theory of MI, in the linear stage of MI, the wave number Q located between

$$-\sqrt{5} \leq Q \leq \sqrt{5} \tag{45}$$

would be unstable, and grow exponentially, expect for $Q = 0$, while the wave number Q outside this range do not change with time.

The asymptotic steady state of S_k is shown in figure 9, where certain regions exhibit power-law decay while others exhibit exponential decay. Overall, the asymptotic steady state of S_k is asymmetric, a feature does not observed in the integrable turbulence of the NLS equation [18, 19]. Before proceeding with the detailed analysis, it is important to first elucidate the underlying factors that give rise to anisotropy. This is primarily due to the selection of the wave number $k = -3$, which is not centered within Eq. (45). Specifically, during the linear stage of MI development, the wave numbers described by Eq. (45) become excited unless $Q = 0$. In the nonlinear stage, other wavenumbers are also excited, but the majority of the wave-action spectrum remains concentrated around the linearly excited MI wavenumbers and near $k = -3$. This results in anisotropy. In contrast, for the NLS case [18, 19], their chosen wave number $k = 0$ coincides with the center of the MI wave number range, leading to an symmetric result.
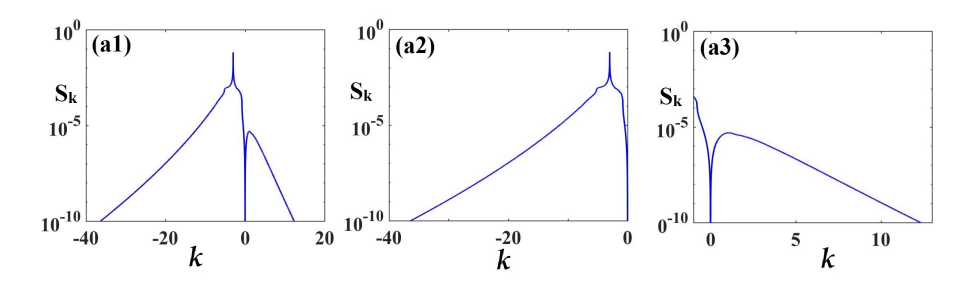
13

Figure 9: The asymptotic wave-action spectrum Eq. (41) with wave number k between $(-40, 20)$ at ($a1$). The zoomed-in images of panel ($a1$) are respectively located at the vicinity of $[-40, 0]$ at ($a2$), while ($a3$) corresponds to $[-1, 13]$.

Next, we will conduct a detailed examination of asymptotic wave-action spectrum S_k in each region. To begin with, we adopt the following functional form to model the power-law decay region:

$$S_k = C|k+3|^{-\alpha}. \tag{46}$$

As for the exponentially decaying region, we employ the following functional representation:

$$S_k = De^{-\beta|k+3|}. \tag{47}$$

It is worth noting that the parameters $\{C, D, \alpha, \beta\}$ vary across different regions. However, for simplicity, we will refrain from introducing separate parameters for each region:

- The first region is near $k = -3$, spanning $[-3.5, -2.5]$, and exhibits power-law decay, as shown in figure. 10($a1$,$a2$). In figure 10($a1$), we consider a global fit and obtain the parameters $C = 9.061 \times 10^{-4}$ and $\alpha = 0.667$. However, we find that splitting the fit on either side of $k = -3$ yields better results (see figure 10($a2$)). On the left side, the parameters are $C = 9.856 \times 10^{-4}$ and $\alpha = 0.638$, while on the right side, the corresponding parameters are $C = 8.332 \times 10^{-4}$ and $\alpha = 0.694$. We believe that this anisotropy can be mitigated by improving the computational environment (e.g., larger ensemble sizes, extended spatial domains).

- The first part of the second region is $k \in [-5.1, -3.5]$, shown in the left part of figure 10($a3$), where the fitting parameters are $C = 1.114 \times 10^{-3}$ and $\alpha = 0.392$. The second part of the second region is $k \in [-2.5, -1.2]$, displayed in the right part of figure 10($a3$), with fitting parameters $C = 8.189 \times 10^{-4}$ and $\alpha = 0.677$. In fact, the second region also appear in the NLS case [18, 19]. However, in that context, the wave-action spectrum across these segments is uniform, while here it exhibits anisotropy. This discrepancy arises primarily because the part $k \in [-2.5, -1.2]$ lies closer to $k = 0$. Since $k = 0$ remains stable in both the linear and nonlinear stages of MI, this segment exhibits a steeper decay. By contrast, in the NLS case, such anisotropy does not occur because the plane wave they consider is already centered at $k = 0$.

- In the third region, S_k exhibits exponential decay, as shown in figure 10($a4$). The first segment, spanning $k \in [-20, -5.1]$, is characterized by the fitted parameters $D = 1.463 \times 10^{-3}$ and $\beta = 0.577$. The second segment, $k \in [-0.8, -0.1]$, yields the parameters $D = 2.222 \times 10^{-3}$ and $\beta = 7.689$, which represents a much faster decay compared to the first segment. This more rapid decay is primarily due to the proximity to the wave number $k = 0$, which remains stable throughout the entire process.

14

Parameters Wave number	$[C, \alpha]$	$[D, \beta]$
$[-3.5, -2.5]$	$[9.061 \times 10^{-4}, 0.667]$	None
$[-5.1, -3.5]$	$[1.114 \times 10^{-3}, 0.392]$	None
$[-2.5, -1.2]$	$[8.189 \times 10^{-4}, 0.677]$	None
$[-20, -5.1]$	None	$[1.463 \times 10^{-3}, 0.577]$
$[-0.8, -0.1]$	None	$[2.222 \times 10^{-3}, 7.689]$
$[1.1, 2.6]$	$[2.139 \times 10^{-4}, 2.645]$	None
$[2.6, 12]$	None	$[8.192 \times 10^{-4}, 1.038]$

Table 1: The fitting parameters in different regions. The first column corresponds to the wave number range. The second column contains the parameters for power-law decay (see Eq.(46)), while the third column lists the parameters for exponential decay (see Eq.(47)), where none represents the wave-action spectrum does not correspond to this type of function.

- The fourth region, corresponding to $k \in [1.1, 2.6]$ (see figure 10(a5)), exhibits power-law decay, with fitted parameters $C = 2.139 \times 10^{-4}$ and $\alpha = 2.645$. This region has not been observed in the NLS case, and its emergence is primarily attributed to the wave number range of the linear MI described by Eq. (45).

- The fifth region, spanning $k \in [2.6, 12]$ (see figure 10(a6)), demonstrates exponential decay, characterized by the parameters $D = 8.192 \times 10^{-4}$ and $\beta = 1.038$.

These results for the wave-action spectrum of the asymptotic steady state are summarized in Table 1.

During the linear phase of MI, and for an extended period in the nonlinear phase, the wave-action spectrum exhibits a discontinuity at $k = -3$, manifested as a prominent peak that occupies only the $k = -3$ harmonic, as shown in figure 11(a1). This peak arises from the initial conditions Eq. (24). Notably, while this peak does not vanish completely in the nonlinear phase, rather than it decays in an oscillatory manner. We also measure the peak by calculating the difference between the harmonic at $k = -3$ and the arithmetic average of the two neighboring harmonics:

$$h(t) = S_{-3}(t) - \frac{1}{2} \left[S_{-3+2\pi/L}(t) + S_{-3-2\pi/L}(t) \right]. \tag{48}$$

It can be observed that $h(t)$ also evolutions as an oscillatory manner with approaching its asymptotic value from figure 11(a2). At the same time, we observe that $S_{-3}(t)$ and $h(t)$ are in anti-phase with $|\langle H_4 \rangle|$.

Next, we specifically examine $S_k(t)$ at the moments corresponding to the strongest and weakest nonlinearity, which occur at $t = 6.4$ and $t = 7.3$, respectively, as depicted in figure 11(b1,b2). One can easily observe that at $t = 6.4$, S_k exhibits more peaks compared to one for $t = 7.3$.

A more advanced statistical measure related to the wave-action spectrum is the autocorrelation function, which can be expressed as [18,19,22,28,96]

$$g(x,t) = \left\langle \frac{1}{L} \int_{-L/2}^{L/2} \psi^*(\eta - x, t) \psi(\eta, t) \, d\eta \right\rangle, \tag{49}$$

which serves as a descriptor of turbulence correlations over spatial separations. This measure is instrumental in characterizing spatial coherence, fluctuation patterns, and the underlying dynamics of energy
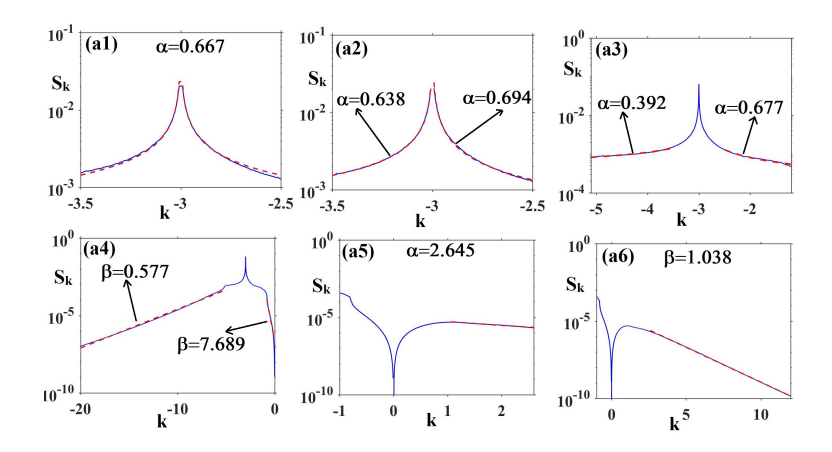
Figure 10: The asymptotic wave-action spectrum Eq. (41) fitting by different functions in different regions. The parameters of algebraic decay Eq. (46): (*a1*) $C = 9.061 \times 10^{-4}$ and $\alpha = 0.667$; (*a2*) Left part with $C = 9.856 \times 10^{-4}$ and $\alpha = 0.638$, right part with $C = 8.332 \times 10^{-4}$ and $\alpha = 0.694$; (*a3*) Left part with $C = 1.114 \times 10^{-3}$ and $\alpha = 0.392$, right part with $C = 8.189 \times 10^{-3}$ and $\alpha = 0.677$; (*a5*) $C = 2.139 \times 10^{-4}$ and $\alpha = 2.645$. The parameters of exponential decay Eq. (47): (*a4*) Left part with $D = 1.463 \times 10^{-3}$ and $\beta = 0.577$, right part with $D = 2.222 \times 10^{-3}$ and $\beta = 7.689$; (*a6*) $D = 8.192 \times 10^{-4}$ and $\beta = 1.038$. In all panels, the solid blue line represents the asymptotic S_k, where the dashed red line denote the fitting result.
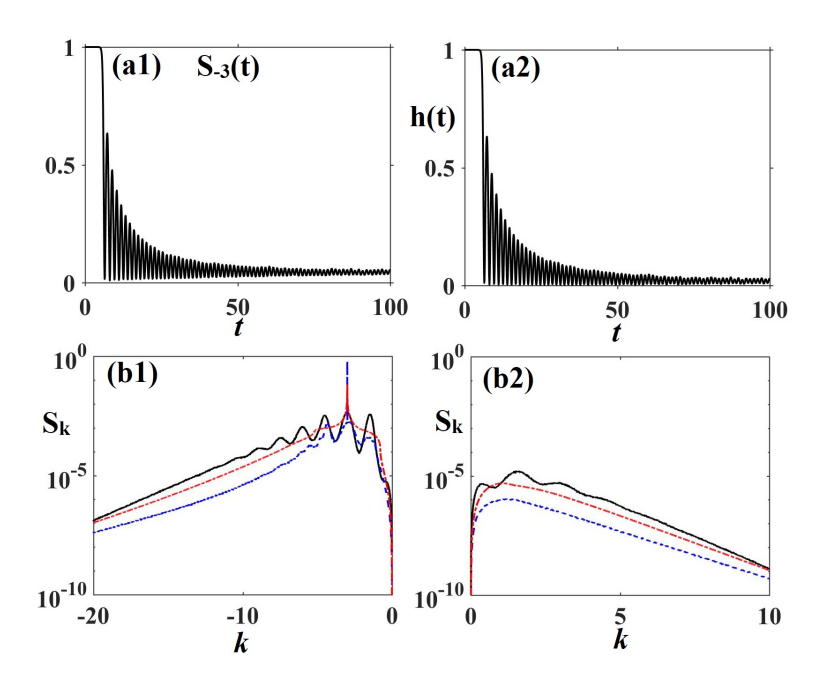

Figure 11: (*a1*) The evolution of the wave-action spectrum at $k = -3$, i.e., $S_{-3}(t)$. (*a2*) The evolution of the peak at $k = -3$ harmonic $h(t)$. (*b1,b2*) The wave-action spectrum function $S_k(t)$ is presented at three specific points: at $t = 6.4$, corresponding to the first local maximum of the ensemble-averaged potential energy modulus $|\langle H_4 \rangle|$ (solid black line); at $t = 7.3$, corresponding to the first local minimum of $|\langle H_4 \rangle|$ (dashed blue line); and as the asymptotic spatial correlation function (dash-dot red line).

16

Figure 12: (*a1*) The asymptotic auto-correlation function $g(x)$. (*a2*) The asymptotic auto-correlation function $g(x)$ fitting by function $e^{-\frac{x}{2\sigma^2}}$ with $\sigma = 0.935$. (*b1*) Evolution of spatial correlation function $g(x,t)$ at $x = 0$ (blue), $x = \pi/2$ (red), $x = \pi$ (yellow), $x = 2\pi$ (purple). (*b2*) The spatial correlation function $g(x,t)$ is presented at three specific points: at $t = 6.4$, corresponding to the first local maximum of the ensemble-averaged potential energy modulus $|\langle H_4 \rangle|$ (solid black line); at $t = 7.3$, corresponding to the first local minimum of $|\langle H_4 \rangle|$ (dashed blue line); and as the asymptotic spatial correlation function (dash-dot red line).
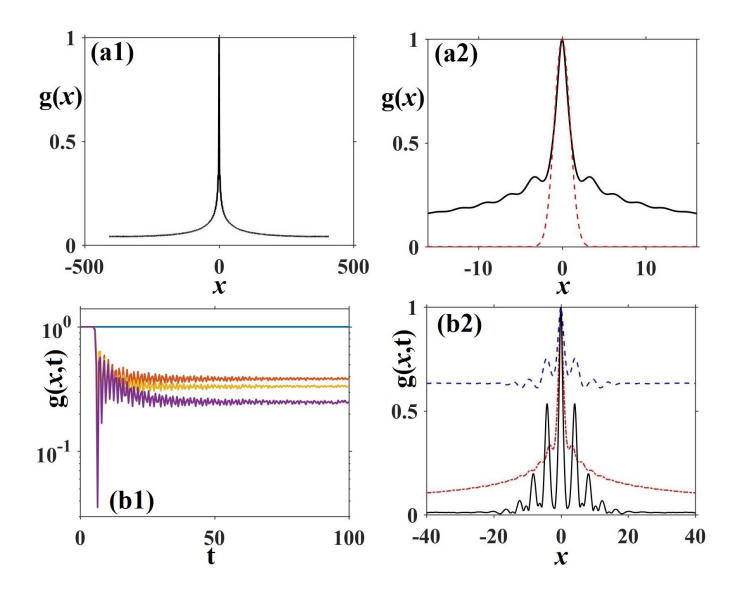
distribution, mixing, and structural development in turbulent systems. Furthermore, the autocorrelation function is directly linked to the wave-action spectrum through the inverse Fourier transform:

$$g(x,t) = \mathcal{F}_D^{-1}\left(S_k(t)\right). \tag{50}$$

The asymptotic auto-correlation function $g(x)$ is depicted in figure 12(*a1*). It is noted that $g(x,t) = 1$ at $x = 0$ for all $t > 0$, primarily because

$$g(0,t) = \left\langle \frac{1}{L} \int_{-L/2}^{L/2} |\psi(\eta,t)|^2 \, d\eta \right\rangle = \langle N \rangle = 1, \tag{51}$$

where the last equality comes from the fact that mass N is a conserved quantity. One notable feature of the spatial correlation function is that it remains at a distinct, nonzero value as $|x| \to L/2$. This phenomenon is observed not only during the linear phase of the MI, but also persists for an extended duration into the nonlinear phase. Such behavior arises from the prominent peak at the $k = -3$ harmonic in the wave-action spectrum S_k. However, for $|x| < 1.15$, the asymptotic $g(x)$ can be well approximated by the following Gaussian function:

$$g(x) \approx \exp\left(-\frac{x^2}{2\sigma^2}\right) \tag{52}$$

with $\sigma = 0.935$ (see figure 12(*a2*)).

For the given x, we display the time evolution of $g(x,t)$ depicted in figure 12(*b1*) for different x. Similarly, we observe that its evolution also oscillates, approaching to their asymptotic values. Although the

oscillations here appear somewhat irregular, we have reason to believe that as the number of ensembles increases, the oscillation pattern will become inversely related to the absolute value of the ensemble-averaged potential energy, $|\langle H_4 \rangle|$. It should be noted that, during the linear MI stage (up to $t \approx 5$), we have

$$g(x,t) \approx 1, \tag{53}$$

which is mainly due to $|\psi(x,t)| \approx 1$. We then also examine the auto-correlation function $g(x)$ at the first local maximum and minimum of the ensemble-averaged potential energy modulus $|\langle H_4 \rangle|$, as shown in figure 12(b2). We observe that at $t = 6.4$, $g(x)$ exhibits more peaks compared to $t = 7.3$, which is also determined by the characteristics of PDF (see figure 7(a1,a2)).

4   Conclusions and discussions

In conclusion, our study of IT phenomena and RW emergence within the DNLSE provides valuable insights into their dynamics. We begin with a plane wave perturbed by a small noise, which led to an in-depth analysis of stationary turbulence using various statistical measures. Moreover, during the evolution of these statistical indices, they consistently oscillate and approach their asymptotic values. The asymptotic form can generally be expressed in a unified manner (see Eqs. (34) and (36)). Notably, we found that, unlike the symmetric turbulence observed in the NLSE, the DNLSE exhibits the asymmetric turbulence, where the energy spectrum shows different power-law decay in different regions. This is primarily due to the asymmetric between the wave number of the plane wave from the MI and the perturbation wave number.

As for potential directions for extending this research, several avenues warrant consideration. First, it would be valuable to explore whether other initial value excitations of IT could be considered, which might generate higher amplitude RWs, such as the coherent initial conditions proposed in work [25]. Second, it would be interesting to investigate whether these phenomena similar to intermittency [39], often observed in fluid turbulence [1, 2], could occur in the IT of the DNLSE. Finally, to the best of our knowledge, there has been no systematic study of IT in higher-dimensional systems, such as the (2+1)-dimensional KP-1 equation.

Appendix A. Numerical Method for the DNLS Eq. (3)
In this work, we primarily employ the fourth-order split-step [45] method for numerical experiments. Specifically, the DNLS Eq. (3) can be split into the following linear and nonlinear parts:

$$\psi_t = (L + N)\psi \tag{A.1}$$

where $L\psi = i\psi_{xx}$ and $N\psi = -\beta(|\psi|^2\psi)_x$. Generally speaking, the split-step algorithm can be formulated as

$$\exp\left(dt(L+N)\right) \approx \prod_{k=1}^{n} \exp(\beta_k dt N) \exp(\alpha_k dt L), \tag{A.2}$$

where dt represents the time step size, and β_k, α_k ($k = 1, 2, \ldots, n$) denote the step coefficients for the nonlinear and linear operators, respectively. Here we adopt a fourth-order split-step algorithm, i.e., $n = 4$ in the general formulation.

In this case, the split equations to be solved are

$$v_t = L(v) \tag{A.3}$$

$$v_t = N(v). \tag{A.4}$$

Here the split equation $v_t = L(v)$ can be solved by the discrete Fourier transform, and the split equation $v_t = N(v)$ has the exact solution formula

$$v(x,t) = v(x,0) \exp\left(-i\beta(2v_x v^* + vv_x^*)t\right) \tag{A.5}$$

for the DNLS equation. During the numerical experiments, we monitor conserved quantities such as the L^2-norm Eq. (12) and the Hamiltonian Eq. (9) to ensure the stability of the numerical algorithm.

Author Contributions All authors contributed to the research and preparation of this work.

Data Availability No new data were created or analysed in this work.

Declarations
Conflict of interest The authors declare no conflict of interest.

References

[1] Nazarenko S 2011 *Wave Turbulence* (Springer)

[2] Zakharov V E, L'vov V S and Falkovich G 2012 *Kolmogorov Spectra of Turbulence I: Wave Turbulence* (Springer Science and Business Media)

[3] Galtier S 2022 *Physics of Wave Turbulence* (Cambridge University Press)

[4] Newell A C and Rumpf B 2011 Wave turbulence *Annu. Rev. Fluid Mech.* **43** 59–78

[5] Collot C, Dietert H and Germain P 2024 Stability and cascades for the Kolmogorov-Zakharov spectrum of wave turbulence *Arch. Rational Mech. Anal.* **248** 7

[6] Zhang Z and Pan Y 2022 Numerical investigation of turbulence of surface gravity waves *J. Fluid. Mech.* **933** A58

[7] Hrabski A and Pan Y 2022 On the properties of energy flux in wave turbulence *J. Fluid Mech.* **936** A47

[8] Griffin A, Krstulovic G, L'vov V S and Nazarenko S 2022 Energy spectrum of two-dimensional acoustic turbulence *Phys. Rev. Lett.* **128** 224501

[9] Lanchon N and Cortet P P 2023 Energy spectra of nonlocal internal gravity wave turbulence *Phys. Rev. Lett.* **131** 264001

[10] Galtier S 2023 A multiple time scale approach for anisotropic inertial wave turbulence *J. Fluid Mech.* **974** A24

[11] Korotkevich A O, Nazarenko S V, Pan Y and Shatah J 2024 Non-local gravity wave turbulence in presence of condensate *J. Fluid Mech.* **992** A1

[12] Kochurin E A and Kuznetsov E A 2024 Three-Dimensional Acoustic Turbulence: Weak Versus Strong *Phys. Rev. Lett.* **133** 207201

[13] Majda A J, McLaughlin D W and Tabak E G 1997 A one-dimensional model for dispersive wave turbulence *J. Nonlinear Sci.* **7** 9–44

[14] Buckmaster T, Germain P, Hani Z and Shatah J 2021 Onset of the wave turbulence description of the longtime behavior of the nonlinear Schrödinger equation *Invent. Math.* **225** 787–855

[15] Zakharov V E 2009 Turbulence in integrable systems *Stud. Appl. Math.* **122** 219

[16] Simonis A and Pan Y 2024 Transition from weak turbulence to collapse turbulence regimes in the Majda-McLaughlin-Tabak model *Phys. Rev. E* **110** 024202

[17] Ying L H, Zhuang Z, Heller E J and Kaplan L 2011 Linear and nonlinear rogue wave statistics in the presence of random currents *Nonlinearity* **24** R67–87

[18] Agafontsev D S and Zakharov V E 2015 Integrable turbulence and formation of rogue waves *Nonlinearity* **28** 2791

[19] Agafontsev D S and Zakharov V E 2016 Integrable turbulence generated from modulational instability of cnoidal waves *Nonlinearity* **29** 3551

[20] Akhmediev N, Soto-Crespo J M and Devine N 2016 Breather turbulence versus soliton turbulence: Rogue waves, probability density functions, and spectral features *Phys. Rev. E* **94** 022212

[21] El G A, Khamis E G and Tovbis A 2016 Dam break problem for the focusing nonlinear Schrödinger equation and the generation of rogue waves *Nonlinearity* **29** 2798–815

[22] Agafontsev D S, Randoux S and Suret P 2021 Extreme rogue wave generation from narrowband partially coherent waves *Phys. Rev. E* **103** 032209

[23] Congy T, El G A, Roberti G, Tovbis A, Randoux S and Suret P 2024 Statistics of extreme events in integrable turbulence *Phys. Rev. Lett.* **132** 207201

[24] Costa A, Osborne A R, Resio D T, Alessio S, Chrivi E, Saggese E, Bellomo K and Long C E 2014 Soliton turbulence in shallow water ocean surface waves *Phys. Rev. Lett.* **113** 108501

[25] Gelash A A and Agafontsev D S 2018 Strongly interacting soliton gas and formation of rogue waves *Phys. Rev. E* **98** 042210

[26] Gelash A A, Agafontsev D S, Zakharov V, El G, Randoux S and Suret P 2019 Bound state soliton gas dynamics underlying the spontaneous modulational instability *Phys. Rev. Lett.* **123** 234102

[27] Koussaifi R E, Tikan A, Toffoli A, Randoux S, Suret P and Onorato M 2018 Spontaneous emergence of rogue waves in partially coherent waves: A quantitative experimental comparison between hydrodynamics and optics *Phys. Rev. E* **97** 012208

[28] Kraych A E, Agafontsev D, Randoux S and Suret P 2019 Statistical properties of the nonlinear stage of modulation instability in fiber optics *Phys. Rev. Lett.* **123** 093902

[29] Li M, Zhu X Z and Xu T 2024 Integrable turbulence and statistical characteristics of chaotic wave field in the Kundu-Eckhaus equation *Phys. Rev. E* **109** 014204

[30] Onorato M, Proment D, El G, Randoux S and Suret P 2016 On the origin of heavy-tail statistics in equations of the nonlinear Schrödinger type *Phys. Lett. A* **380** 3173

[31] Osborne A R, Resio D T, Costa A, Ponce de León S and Chirivi E 2019 Highly nonlinear wind waves in Currituck Sound: Dense breather turbulence in random ocean waves *Ocean Dyn.* **69** 187–219

[32] Redor I, Barthélemy E, Mordant N and Michallet H 2020 Analysis of soliton gas with large-scale video-based wave measurements *Exp. Fluids* **61** 1–14

[33] Roberti G, El G, Randoux S and Suret P 2019 Early stage of integrable turbulence in the one-dimensional nonlinear Schrödinger equation: A semiclassical approach to statistics *Phys. Rev. E* **100** 032212

[34] Soto-Crespo J M, Devine N and Akhmediev N 2016 Integrable turbulence and rogue waves: Breathers or solitons? *Phys. Rev. Lett.* **116** 103901

[35] Sun Z Y, Yu X and Feng Y J 2023 Coexistence of Gaussian and non-Gaussian statistics in vector integrable turbulence *Phys. Rev. E* **108** 054211

[36] Suret P, Koussaifi R E, Tikan A, Evain C, Randoux S, Szwaj C and Bielawski S 2016 Single-shot observation of optical rogue waves in integrable turbulence using time microscopy *Nat. Commun.* **7** 13136

[37] Suret P, Randoux S, Gelash A, Agafontsev D S, Doyon B and El G A 2024 Soliton gas: Theory, numerics, and experiments *Phys. Rev. E* **109** 061001

[38] Suret P, Tikan A, Bonnefoy F, Copie F, Ducrozet G, Gelash A, Prabhudesai G, Michel G, Cazaubiel A, Falcon E, El G and Randoux S 2020 Nonlinear spectral synthesis of soliton gas in deep-water surface gravity waves *Phys. Rev. Lett.* **125** 264101

[39] Randoux S, Walczak P, Onorato M and Suret P 2014 Intermittency in integrable turbulence *Phys. Rev. Lett.* **113** 113902

[40] Tikan A, Bielawski S, Szwaj C, Randoux S and Suret P 2018 Single-shot measurement of phase and amplitude by using a heterodyne time-lens system and ultrafast digital timeholography *Nat. Photon.* **12** 228

[41] Walczak P, Randoux S and Suret P 2015 Optical rogue waves in integrable turbulence *Phys. Rev. Lett.* **114** 143903

[42] Zhong M, Weng W, Guo B and Yan Z 2025 The fractional nonlinear Schrödinger equation: Soliton turbulence, modulation instability, and extreme rogue waves *Chaos* **35** 013131

[43] Fibich G 2015 *The Nonlinear Schrödinger Equation: Singular Solutions and Optical Collapse* Springer

[44] Peregrine D H 1983 Water waves, nonlinear Schrödinger equations and their solutions *J. Aust. Math. Soc. Ser. B* **25** 16–43

[45] YANG J 2010 *Nonlinear Waves in Integrable and Nonintegrable Systems* (SIAM)

[46] Rogister A 1971 Parallel propagation of nonlinear low-frequency waves in high-β plasma *Phys. Fluids* **14** 2733–2739

[47] Bahouri H and Perelman G 2022 Global well-posedness for the derivative nonlinear Schrödinger equation *Invent. Math.* **229** 639–688

[48] Ichikawa Y H and Watanabe S 1977 Solitons, envelope solitons in collisionless plasmas, Third international congress: waves and instabilities in plasmas *J. Phys. Colloques* **38** 15–26

[49] Kaup D J and Newell A C 1978 An exact solution for a derivative nonlinear Schrödinger equation *J. Math. Phys.* **19** 798

[50] Killip R, Ntekou M and Visan M 2023 On the well-posedness problem for the derivative nonlinear Schrödinger equation *Analysis & PDE* **16** 1245–1270

[51] Mio K, Ogino T, Minami K, Takeda S 1976 Modified nonlinear Schrödinger equation for Alfvén waves propagating along the magnetic field in cold plasmas *J. Phys. Soc. Japan* **41** 265–271

[52] Mjølhus E 1976 On the modulational instability of hydromagnetic waves parallel to the magnetic field *J. Plasma Phys.* **16** 321–334

[53] Mjølhus E 1989 Nonlinear Alfvén waves and the DNLS equation: oblique aspects *Phys. Scr.* **40** 227

[54] Nakata I 1991 Weak nonlinear electromagnetic waves in a ferromagnet propagating parallel to an external magnetic field *J. Phys. Soc. Japan* **60** 3976–3977

[55] Daniel M and Veerakumar V 2002 Propagation of electromagnetic soliton in antiferromagnetic medium *Phys. Lett. A* **302** 77–86

[56] Nakata I, Ono H and Yosida M 1993 Solitons in a dielectric medium under an external magnetic field *Prog. Theor. Phys.* **90** 739–742

[57] Chen X J and Lam W K 2004 Inverse scattering transform for the derivative nonlinear Schrödinger equation with nonvanishing boundary conditions *Phys. Rev. E* **69** 066604

[58] Lashkin V 2007 N-soliton solutions and perturbation theory for the derivative nonlinear Schrödinger equation with nonvanishing boundary conditions *J. Phys. A: Math. Theor.* **40** 6119

[59] Xu S, He J and Wang L 2011 The Darboux transformation of the derivative nonlinear Schrödinger equation *J. Phys. A: Math. Theor.* **44** 305203

[60] Zhang G and Yan Z 2020 The derivative nonlinear Schrödinger equation with zero/nonzero boundary conditions: Inverse scattering transforms and N-double-pole solutions *J. Nonlinear Sci.* **30** 3089–3127

[61] Zhou G 2012 A newly revised inverse scattering transform for DNLS+ equation under nonvanishing boundary condition *Wuhan Univ. J. Nat. Sci.* **17** 144–150

[62] Copie F, Randoux S and Suret P 2020 The Physics of the one-dimensional nonlinear Schrödinger equation in fiber optics: Rogue waves, modulation instability and self-focusing phenomena *Rev. Phys.* **5** 100037

[63] Benjamin T B and Feir J E 1967 The disintegration of wave trains on deep water part 1. Theory *J. Fluid Mech.* **27** 417–430

[64] Zakharov V E and Gelash A A 2013 Nonlinear stage of modulation instability *Phys. Rev. Lett.* **111** 054101

[65] Närhi M, Wetzel B, Billet C, Toenger S, Sylvestre T, Merolla J-M, Morandotti R, Dias F, Genty G and Dudley J M 2016 Real-time measurements of spontaneous breathers and rogue wave events in optical fibre modulation instability *Nat. Commun.* **7** 13675

[66] Akhmediev N, Ankiewicz A and Taki M 2009 Waves that appear from nowhere and disappear without a trace *Phys. Lett. A* **373** 675-678

[67] Solli D R, Ropers C, Koonath P and Jalali B 2007 Optical rogue waves *Nature* **450** 1054-1057

[68] Akhmediev N,Soto-Crespo J M and Ankiewicz A 2009 Extreme waves that appear from nowhere: On the nature of rogue waves *Phys. Lett. A* **373** 2137-2145

[69] Chabchoub A, Hoffmann N P and Akhmediev N 2011 Rogue wave observation in a water wave tank *Phys. Rev. Lett.* **106** 204502

[70] Dysthe K,Krogstad H E and Müller P 2008 Oceanic rogue waves *Annu. Rev. Fluid Mech.* **40** 287-310

[71] Fedele F 2008 Rogue waves in oceanic turbulence *Physica D* **237** 2127-2131

[72] Kharif C and Pelinovsky E 2003 Physical mechanisms of the rogue wave phenomenon *Eur. J. Mech. B. Fluids* **22** 603-634

[73] Chen J and Pelinovsky D E 2018 Rogue periodic waves of the modified KdV equation *Nonlinearity* **31** 1955–80

[74] Rao J, Zhang Y, Fokas A S and He J 2018 Rogue waves of the nonlocal Davey–Stewartson I equation *Nonlinearity* **31** 4090–107

[75] Li Y, Draycott S, Zheng Y, Lin Z, Adcock T A and van den Bremer T S 2021 Why rogue waves occur atop abrupt depth transitions *J. Fluid Mech.* **919** R5

[76] Mendes S and Kasparian J 2023 Non-homogeneous approximation for the kurtosis evolution of shoaling rogue waves *J. Fluid Mech.* **966** A42

[77] Li R, Geng J and Geng X 2024 Breather and rogue-wave solutions of the semi-discrete and continuous nonlinear Schrödinger equations on theta-function backgrounds *Nonlinearity* **38** 015012

[78] Mendes S, Teutsch I and Kasparian J 2025 Symmetric influence of forward and opposing tidal currents on rogue wave statistics *J. Fluid Mech.* **1012** A22

[79] Onorato M, Residori S, Bortolozzo U, Montina A and Arecchi F T 2013 Rogue waves and their generating mechanisms in different physical contexts *Phys. Rep.* **528** 47-89

[80] Tang T, Barratt D, Bingham H B, van den Bremer T S, Adcock T A 2022 The impact of removing the high-frequency spectral tail on rogue wave statistics *J. Fluid Mech.* **953** A9

[81] Toffoli A, Waseda T, Houtani H, Cavaleri L, Greaves D and Onorato M 2015 Rogue waves in opposing currents: an experimental study on deterministic and stochastic wave trains *J. Fluid Mech.* **769** 277-297

[82] Xiao W, Liu Y, Wu G and Yue D K 2013 Rogue wave occurrence and dynamics by direct simulations of nonlinear wave-field evolution *J. Fluid Mech.* **720** 357-392

[83] Zhang J, Mendes S, Benoit M and Kasparian J 2024 Effect of shoaling length on rogue wave occurrence *J. Fluid Mech.* **997** A69

[84] Akhmediev N and Pelinovsky E 2010 Editorial-introductory remarks on discussion & debate: Rogue waves-towards a unifying concept? *Eur. Phys. J. Spec. Top.* **185** 1-4

[85] Kibler B, Fatome J, Finot C, Millot G, Dias F, Genty G, Akhmediev N and Dudley J M 2010 The Peregrine soliton in nonlinear fibre optics *Nat. Phys.* **6** 790-795

[86] Ganshin A N, Efimov V B, Kolmakov G V, Mezhov-Deglin L P and McClintock P V E 2008 Observation of an inverse energy cascade in developed acoustic turbulence in superfluid Helium *Phys. Rev. Lett.* **101** 065303

[87] Bailung H, Sharma S K and Nakamura Y 2011 Observation of Peregrine solitons in a multicomponent plasma with negative ions *Phys. Rev. Lett.* **107** 255005

[88] Moslem W M 2011 Langmuir rogue waves in electron-positron plasmas *Phys. Plasmas* **18** 032301

[89] Bludov Y, Konotop V and Akhmediev N 2009 Matter rogue waves *Phys. Rev. A* **80** 33610

[90] Yan Z, Konotop V and Akhmediev N 2010 Three-dimensional rogue waves in nonstationary parabolic potentials *Phys. Rev. E* **82** 036610

[91] Laveder D, Passot T T, Sulem P and Sánchez-Arriaga G 2011 Rogue waves in Alfvénic turbulence *Phys. Lett. A* **375** 3997-4002

[92] Yan Z 2010 Financial rogue waves *Commun. Theor. Phys.* **54** 947

[93] Lakoba T I 2015 Effect of noise on extreme events probability in a one-dimensional nonlinear Schrödinger equation *Phys. Lett. A* **379** 1821-1827

[94] Dudley J M, Dias F, Erkintalo M and Genty G 2014 Instabilities, breathers and rogue waves in optics *Nat. Photon.* **8** 755-764

[95] Armaroli A, Conti C and Biancalana F 2015 Rogue solitons in optical fibers: A dynamical process in a complex energy landscape? *Optica* **2** 497-504

[96] Sun Z Y and Yu X 2021 Nearly integrable turbulence and rogue waves in disordered nonlinear Schrödinger systems *Phys. Rev. E* **103** 062203

[97] Wang L and Yan Z 2021 Rogue wave formation and interactions in the defocusing nonlinear Schrödinger equation with external potentials *Appl. Math. Lett.* **111** 106670

[98] Biondini G and Mantzavinos D 2017 Long-time asymptotics for the focusing nonlinear Schrödinger equation with nonzero boundary conditions at infinity and asymptotic stage of modulational instability *Commun. Pure Appl. Math.* **70** 2300-2365